

# Performance analysis of Fast Marching-based motion planning for autonomous mobile robots in ITER scenarios

Javier V. Gómez<sup>a,\*</sup>, Alberto Vale<sup>b</sup>, Santiago Garrido<sup>a</sup>, Luis Moreno<sup>a</sup>

<sup>a</sup>*RoboticsLab., Carlos III University of Madrid, Avda. de la Universidad 30, 28911, Leganés, Madrid, Spain.*

<sup>b</sup>*Instituto de Plasmas e Fusão Nuclear at Instituto Superior Técnico, Universidade de Lisboa, Portugal*

---

## Abstract

Operations of transportation in cluttered environments require robust motion planning algorithms. Specially with large and heavy vehicles under hazardous operations of maintenance, such as in the ITER, an international nuclear fusion research project. The load transportation inside the ITER facilities require smooth and optimized paths with safety margin of 30 cm. The transportation is accomplished by large rhombic-like vehicles to exploit its kinematic capabilities. This paper presents the performance analysis of a motion planning algorithm to optimize trajectories in terms of clearance, smoothness and execution time in cluttered scenarios. The algorithm is an upgraded version of a previous one used in ITER, replacing the initialization implemented using Constrained Delaunay Triangulation by the Fast Marching Square. Exhaustive simulated experiments have been carried out in different levels of ITER buildings, comparing the performance of the algorithm using different metrics.

## *Keywords:*

Motion planning, fast marching square, rigid body dynamics, ITER

---

\*Corresponding author

*Email address:* [jvgomez@ing.uc3m.es](mailto:jvgomez@ing.uc3m.es) (Javier V. Gómez)

*URL:* <http://roboticslab.uc3m.es/> (Javier V. Gómez)

## 1. Introduction

Path planning is one of the key issues for hazardous transport operations using autonomous mobile robots. Not only for scenarios of disaster, but also when working in experimental scenarios testing new sources of energy where human being is not allowed. In particular, the International Thermonuclear Experimental Reactor (ITER) is a worldwide research experiment that aims to explore nuclear fusion as a viable source of energy for the coming years. The ITER project aims to make the long-awaited transition from experimental studies of plasma physics to full-scale electricity-producing fusion power plants. The largest experimental tokamak nuclear fusion reactor, depicted in Figure 1, will be located at the Cadarache facility, in the south of France.

Besides the major scientific objective of exploring the nuclear fusion as a source of energy, ITER aims to demonstrate that the future fusion power plants can be safely and effectively maintained through Remote Handling (RH) techniques, due to restrictions on human being in activated areas. The RH approach must be from the outset as flexible as possible with minimum reliance on the tokamak configuration, such as in ITER, [1].

The top level maintenance functions of RH in ITER are the exchange of blanket segments, divertor cassettes, perform in-vessel inspection and recovery tasks, allow remote maintenance of ex-vessel systems including heating and current drive systems, ex-vessel transfer casks and servo manipulators. In particular, the maintenance functions of ex-vessel transfer cask has a relevant reliance not only with the reactor, but with the entire power plant. Transportation of equipment for storage, refurbishment and repair requires vehicles of transportation that navigate along corridors of the power plant. A transport cask system (simply identified as cask) is required to accomplish the maintenance operations that includes transportation. Pre-computed paths assuming the well-known scenarios are expected for nominal operations. However, during the maintenance operations, new paths must be computed. For instance, when a cask fails, another rescue cask has to dock into the first one, remove the activated load and then drive it to the maintenance area.

The cask, depicted at the bottom of Figure 1, is a large and complex unit to transport heavy and contaminated components between the two main buildings of ITER: the Tokamak Building (TB), where the reactor is installed, and the Hot Cell Building (HCB) for refurbishment and storage. The geometry of the cask and its payload vary according to the components

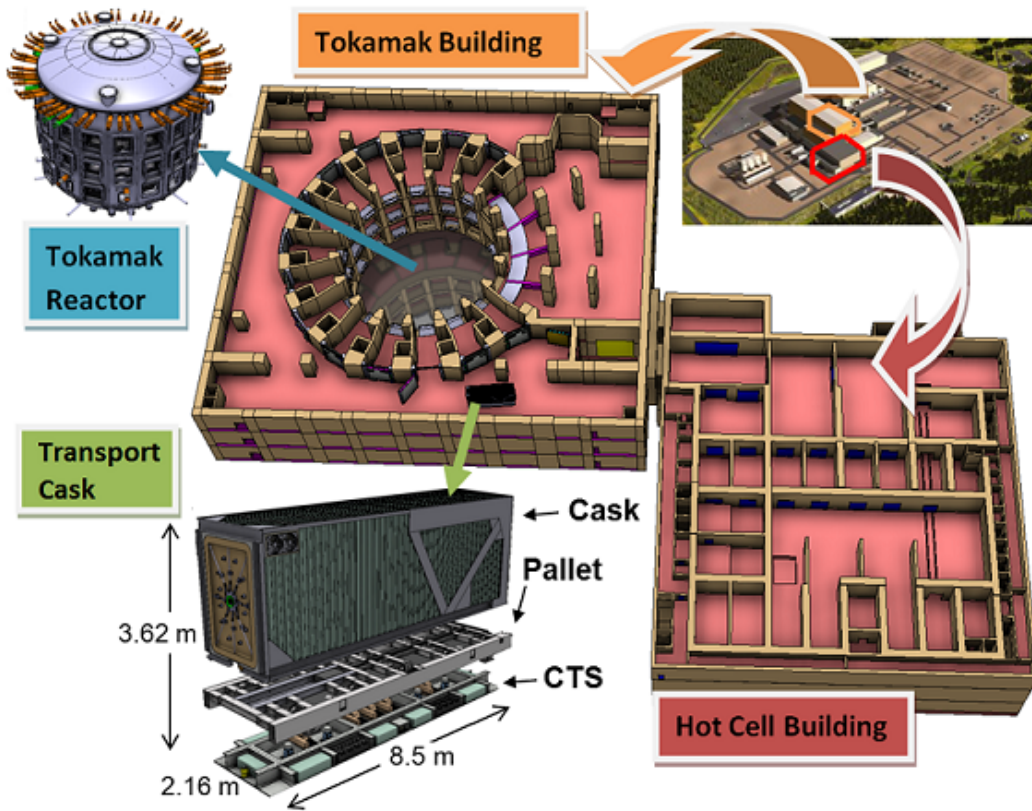


Figure 1: The ITER tokamak and the scientific buildings and facilities that will house the ITER experiments in Cadarache, South of France.

38 to be transported and hence, different cask typologies are expected. As a  
 39 reference, the largest cask dimensions are 8.5m x 2.62m x 3.62m (length x  
 40 width x height) and the total weight can reach up to 100 tons.

41 The maintenance operations of transportation require the cask to move  
 42 throughout the cluttered environments of the TB and the HCB, equivalent  
 43 to drive a truck under 30 cm of safety margins to the closest walls and pil-  
 44 lars. The constrained space may also rise a logistic problem, where multiple  
 45 vehicles have to move and different paths must be computed.

46 The kinematics of the cask are equivalent to a rhombic like vehicle,  
 47 with two drivable and steerable wheels. Given this configuration, proposed  
 48 in [2, 3], the cask has a higher maneuverability in confined spaces than the  
 49 traditional cars with Ackerman or tricycle configurations [4].

50 From previous work of RH in ITER, the optimized paths would be imple-  
51 mented on the scenario using buried wired systems [2]. Presently, the buried  
52 wired systems are being superseded by other systems, as a line painted on  
53 the floor or, simply, by a virtual path. These systems are used in several  
54 Automatic Guided Vehicles (AGV) applications [5, 6, 7]. In this navigation  
55 methodology, the vehicles would follow the path by using a line guidance  
56 approach: both wheels following the same path. The proposed planning  
57 methodology returns directly the path to be followed by the center of the  
58 wheels and not the one corresponding to the center of the vehicle (identified  
59 as the free roaming, out of the scope of this paper).

60 A nominal operation of the vehicle for a specified environment determines  
61 a motion between two configurations (2D points with specific orientations).  
62 The first step of this planning methodology is to find an initial geometric  
63 path, i.e. a set of 2D points, connecting the initial and final configurations.  
64 The previous implemented approach was based on the Constrained Delaunay  
65 Triangulation (CDT) [8, 9]. This solution presents some limitations in terms  
66 of path smoothness. In complex scenarios, the geometric representation re-  
67 sults in a huge number of triangles with rough initial paths still far from  
68 the optimal one, yielding to a computational effort [10]. The Fast March-  
69 ing Square path planning method (FM<sup>2</sup>) [11] is an alternative approach for  
70 the initialization. The FM<sup>2</sup> provides an initial path closer to the optimal  
71 solution and in a shorter period of time, resulting in an improvement of the  
72 computational effort.

73 Previous works have already addressed the application of the Fast March-  
74 ing Method (FMM) to kinematically constrained systems. Concretely, one of  
75 the first approaches is an iterative method which in every iteration computes  
76 a different path [12]. If this path does not satisfy the kinematic constraints,  
77 the obstacles are smoothly dilated, so that the next computed path will have  
78 smoother, larger curves. This process is repeated until a valid path was  
79 found. Another different approach is to compute an initial path with FMM  
80 and then propagate a second FMM wave within a tube in the initial path  
81 surroundings [13, 14]. In this second wave expansion, the FMM is modified  
82 so that neighbors of the grid cell are no longer computing according Von  
83 Neumann neighborhood, but are computed by propagating the system with  
84 different input actions. The main drawback of this problem is its computa-  
85 tional complexity. Ryo et al. [15] proposed a new Hamilton-Jacobi formula-  
86 tion for computing optimal trajectories for systems with limited curvature.  
87 This formulation has been successfully applied to Dubin's and ReedsShepp

88 car models. However, the whole formulation needs to be done from scratch  
89 for every different kinematic system.

90 Authors' previous work in this topic focuses on the application of FM<sup>2</sup> in  
91 a 3-dimensional configuration space (two spatial dimensions and the vehicle  
92 orientation) [16]. When applying FM<sup>2</sup> in this configuration space, smooth  
93 paths are guaranteed. However, this approach did not take into account  
94 explicitly the kinematic constraints. However, in this work the regular 2-  
95 dimensional version is being applied since the vehicle employed (detailed  
96 in section 2.2) do not have kinematic constraints. However, the vehicle's  
97 kinematics and dimensions require a similar study to that carried out in  
98 vehicles with such constraints.

99 During the maintenance operations of transportation, the pose (position  
100 and orientation) of each vehicle must be continuously evaluated using sensors  
101 data. Although the first studies of localization of the CTS in ITER have been  
102 accomplished, as described in [17], in this paper it is assumed that the pose  
103 of the vehicle is always known without any uncertainty.

104 The paper is organized as follows. The Section 2 describes the problem  
105 statement: the scenario, the vehicle, the goals and the optimization criteria.  
106 The Section 3 introduces the FMM and how it is implemented to become  
107 the FM<sup>2</sup>. The Section 4 describes the optimization in terms of clearance  
108 and smoothness applied to the paths returned by the FM<sup>2</sup>. The Section 5  
109 presents simulated results in the ITER scenarios. Conclusions and future  
110 work are pointed out in Section 6.

## 111 2. Problem Statement

112 The problem statement description is divided into four different issues:  
113 the environments, the vehicles, the missions (goals) and the optimization  
114 criteria.

### 115 2.1. Environments

116 The TB, shown in Figure 2, lodges the tokamak reactor with access by  
117 vacuum vessel port cells (from this point forward simply identified as ports).  
118 The HCB, depicted in Figure 3, will work mainly as a support area. A lift  
119 establishes the only interface between the different levels of TB and the HCB.

120 In ITER, the environments in all levels of TB and HCB are mostly com-  
121 posed by static and well structured scenarios. Each level of the buildings is  
122 modeled as 2D map representation,  $M$ , with a set of 2D points,  $p_i$ , on the

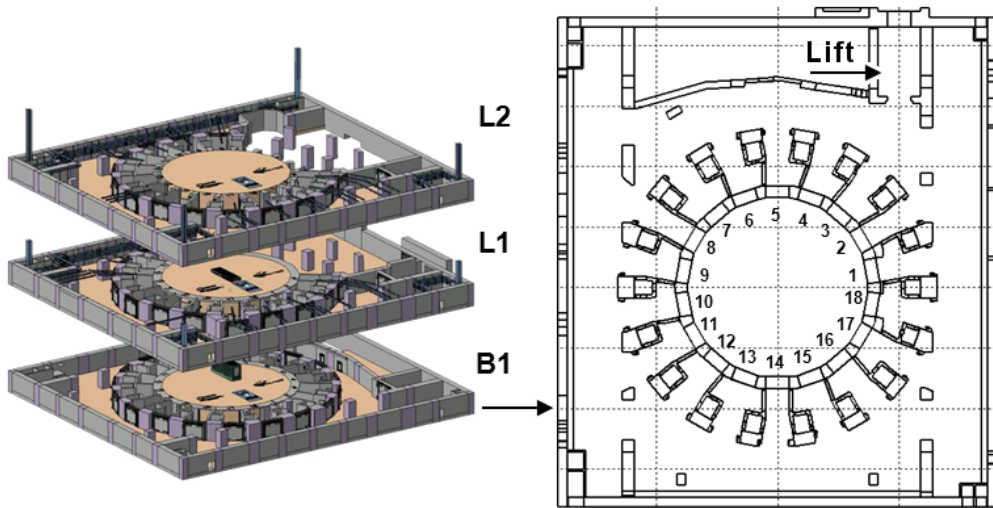


Figure 2: The three main level of Tokamak Building in ITER (left) and the 2D representation of the level B1 (right).

123 global Cartesian referential of ITER and a set line segments,  $l_{jk}$ , where each  
 124 line segment connects two different points  $p_j$  and  $p_k$ , i.e.,

$$M = \{p_i, l_{jk} | i, j, k = 1, \dots, M_p\} \quad (1)$$

125 where  $M_P$  is the number of points,  $p_i = (x, y)$  and  $l_{jk} = \{(1-t) \cdot p_j + t \cdot p_k | t \in$   
 126  $[0, 1]\}$ .

## 127 2.2. Transport cask

128 The vehicle, represented in Figure 1, is a large and complex unit to trans-  
 129 port heavy and contaminated load between the TB and the HCB. The ge-  
 130 ometry of the vehicle and its payload vary according to the cask and the  
 131 components to be transported and hence, different vehicle typologies will  
 132 operate.

133 The vehicle is composed by three sub-systems: the cask envelope, the  
 134 Cask Transfer System (CTS), and the pallet. The cask envelope is a container  
 135 that encloses the in-vessel components and the RH tools to be transported.  
 136 The CTS acts as a mobile robot. The pallet is the interface between the cask  
 137 and the CTS. It is equipped with a handling platform to support the cask  
 138 load and help on docking procedures. When underneath the pallet the CTS

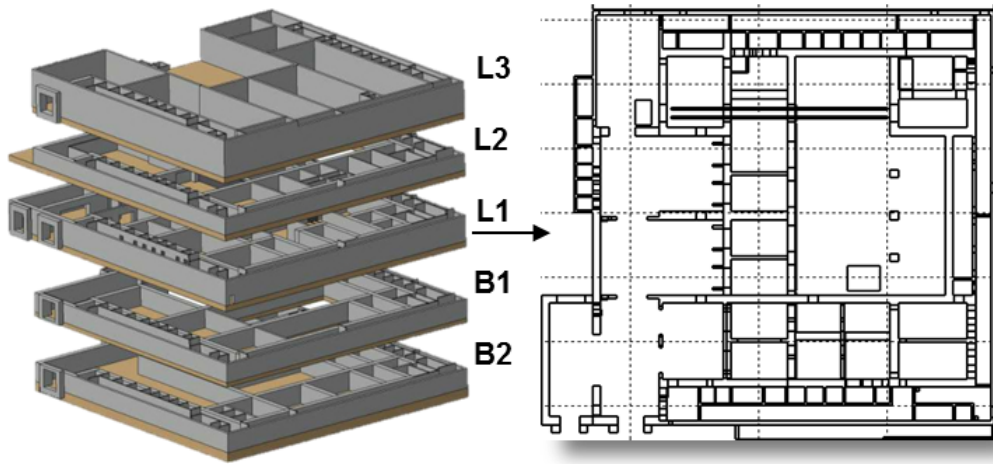


Figure 3: The five main levels of Hot Cell Building in ITER (left) and the 2D representation of the level L1 (right).

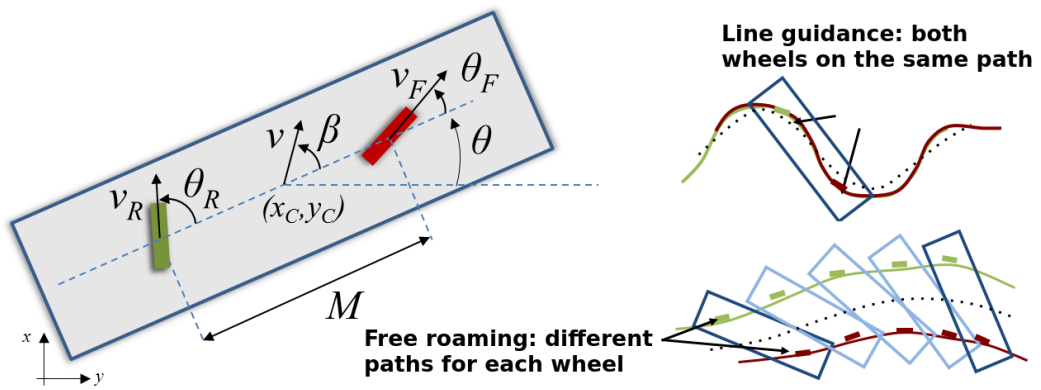


Figure 4: Rhombic vehicle model and the possible path following approaches.

139 transports the cask, but it can also move independently of the pallet and  
 140 cask.

141 The CTS is equipped with two pairs of drivable and steerable wheels:  
 142 one for nominal operation and the other for redundancy, operating in case of  
 143 failure of the first pair, [18]. These locomotion wheels are installed along the  
 144 longitudinal axis the vehicle, providing the rhombic like capabilities. Since  
 145 the locomotion wheels are installed along a straight line, there are free wheels  
 146 in the vicinity of the boundaries of the vehicle’s shape to assure the CTS’s  
 147 stability. For simplicity and from this point forward, the CTS is only rep-  
 148 resented with a single pair of drivable and steerable wheels, identified as  
 149 ‘F’ront and ‘R’ear wheels, as illustrated in Figure 4. This configuration gives  
 150 the vehicle a higher maneuverability in confined spaces than the traditional  
 151 cars with Ackerman or tricycle configurations [4].

152 As illustrated in Figure 4, consider the state vector  $q = [x_c \ y_c \ \theta]$  as a rep-  
 153 resentation of the vehicle pose in the frame  $\{I\}$ , with  $(x_c, y_c)$  the coordinates  
 154 of the center of the vehicle and  $\theta$  the orientation of the vehicle. Also, con-  
 155 sider  $v$  as the longitudinal speed and  $\beta$  the controllable side-slip angle of the  
 156 vehicle, both defined in  $\{I\}$ . A kinematic model for a rhombic like vehicle  
 157 in  $\{I\}$ , that allows the simulation of the vehicle motion directly through the  
 158 desired longitudinal speed  $v$ , instead of imposing an individual linear speed  
 159 for each wheel, was introduced in [19] as:

$$\begin{bmatrix} \dot{x}_c \\ \dot{y}_c \\ \dot{\theta}_m \end{bmatrix} = \begin{bmatrix} \cos(\theta + \beta) \\ \sin(\theta + \beta) \\ \frac{\cos \beta \cdot [\tan \theta_F - \tan \theta_R]}{M} \end{bmatrix} \cdot v, \quad (2)$$

160 where

$$\beta = \arctan \left( \frac{v_F \cdot \sin \theta_F + v_R \cdot \sin \theta_R}{2 \cdot v_R \cdot \cos \theta_R} \right) \quad (3)$$

161 and

$$v = \frac{v_F \cdot \cos \theta_F + v_R \cdot \cos \theta_R}{2 \cdot \cos \beta}. \quad (4)$$

162 This modeling entails that the wheels of the vehicle roll without slipping,  
 163 a constraint inherent to the nonholonomy of rhombic like vehicles, and also  
 164 considers a rigid body constraint, common to this type of vehicles, as follows:

$$v_F \cos \theta_F = v_R \cos \theta_R. \quad (5)$$



165 The values  $v_F$ ,  $v_R$ ,  $\theta_F$  and  $\theta_R$  are the inputs to guide the vehicle, as  
166 detailed in [20].

### 167 2.3. Missions

168 The maintenance operations of transportation in ITER require the vehicle  
169 to move throughout the cluttered environments of the TB and the HCB, i.e.  
170 a mesh of paths between the target poses inside the buildings. For instance, a  
171 mission of transportation of a load for refurbishment requires a path between  
172 a port and the lift in TB and then between the lift and a docking port in  
173 HCB.

### 174 2.4. Optimization criteria

175 During a mission the vehicle describes a swept volume when follow its  
176 path. The volume is important given the free space available in the scenario,  
177 or given other parked vehicles. The speed of the path following is also rel-  
178 evant not only for the mission execution time, but in particularly given the  
179 dynamics of the vehicle, since it can reach up to 100 tons. As a result, each  
180 mission requires an optimized trajectory.

181 The trajectory optimization problem stated for the vehicle consists on  
182 evaluating a trajectory, i.e. a geometric path defined by a set of  $N$  points  
183  $P_i$ , i.e.,  $S = \{P_0, P_1, \dots, P_N\}$ , combined with a speed profile. The geometric  
184 path must guarantee that the vehicle departs from the initial configuration  
185  $q_S$  and achieves the specified goal  $q_F$ , without colliding with obstacles and  
186 keeping a safety margin. The trajectory optimization has three stages: the  
187 geometric path evaluation, the path optimization and the trajectory evalu-  
188 ation. The geometric path evaluation aims to find a path connecting the  
189 initial and goal configurations. This path acts as an initial condition for the  
190 path optimization stage. The geometric path evaluation is implemented using  
191 FM<sup>2</sup>, as described in Section 3. The path optimization receives the preceding  
192 geometric solution as input and returns an optimized path. The optimization  
193 process, described in Section 4, first applies a spline interpolation to satisfy  
194 weaker differential constraints such as smoothness requirements. Afterward,  
195 a clearance based optimization is carried out to guarantee a collision free  
196 path that meets the safety requirements. In general, a minimum safety dis-  
197 tance between the vehicle and the obstacles must be guaranteed. Finally, the  
198 trajectory evaluation defines the velocity function along the optimized path  
199 transforming it into a trajectory, which is the final output.

200 **3. Fast Marching Methods in Path Planning**

201 The FM<sup>2</sup> was firstly introduced by Garrido et al. [11]. Since then, it has  
 202 been successfully applied to many different problems [21] and novel versions  
 203 of the algorithm have been proposed [22]. It consists on applying twice the  
 204 FMM, originally proposed by J.A. Sethian [23]. Both methods are intuitively  
 205 explained in the following subsections.

206 *3.1. The Fast Marching Method*

207 The FMM [23] is an efficient numerical algorithm for modeling a wave  
 208 front evolution through media with different propagation velocities. It is a  
 209 particular case of the level set methods [24] in which the wave always expands  
 210 outwards, that is, with non-negative velocity.

211 The FMM computes the time  $T$  a wave takes in order to reach every  
 212 point of the space using a dynamic programming scheme. Let us assume a  
 213 bi-dimensional grid map. The wave source point  $x_0$  is given a value  $T_0 = 0$ .  
 214 The FMM follows a upwind propagation procedure to solve the wave arrival  
 215 time  $T_{i,j}$  at each point with coordinates  $(i, j)$  according to the discrete Eikonal  
 216 equation [24]:

$$\max\left(\frac{T - T_1}{\Delta x}, 0\right)^2 + \max\left(\frac{T - T_2}{\Delta y}, 0\right)^2 = \frac{1}{F_{i,j}^2} \quad (6)$$

217 where  $\Delta x$  and  $\Delta y$  are the grid spacing in the  $x$  and  $y$  directions,  $F_{i,j}$  is the  
 218 wave propagation speed for grid cell  $(i, j)$  and

$$\begin{aligned} T &= T_{i,j} \\ T_1 &= \min(T_{i-1,j}, T_{i+1,j}) \\ T_2 &= \min(T_{i,j-1}, T_{i,j+1}) \end{aligned} \quad (7)$$

219 The output is a distances map or, more properly, a times-of-arrival map.  
 220 It is possible to have many wave source points, all of them with value  $T = 0$ .

221 When a constant velocity propagation is used the paths, computed as  
 222 geodesics in  $T(x)$ , are optimal in terms of distance but they are not smooth  
 223 and run too close to obstacles. In order to get a more detailed, formal  
 224 description of the FMM, we refer interested readers to [23, 22].

225 *3.2. The Fast Marching Square Path Planning Method*

226 When abrupt changes occur in the wave velocity, geodesics lose their  
227 smoothness. In other words, they become not differentiable when there is a  
228 transition in the wave propagation speed. In fact, it is analogous to geometric  
229 optics and how light rays deform in media with different refraction indices.  
230 In case of a continuous gradient in the velocities map, the path is deformed  
231 smoothly (Figure 5).

232 The FM<sup>2</sup> is a path planning method designed to leverage the continuous  
233 curvature of the paths in the presence of velocities gradients [11]. It is based  
234 on the application of the FMM twice: firstly in order to create a velocities  
235 map of the environment and secondly to compute a path between two given  
236 points. The steps of the algorithm are the following:

- 237 • **Environment**,  $W_0$ : it is represented as a binary grid map in which  
238 obstacles are labeled as 0 (black) and the rest of the space as 1 (white).
- 239 • **Velocities map**,  $F$ : the FMM is applied using all the cells labeled as  
240 obstacles as wave sources. Then, the resulting map is rescaled so that  
241 its values are between 0 and 1. This step is actually the computation  
242 of a smooth distance transform.
- 243 • **Times-of-arrival map**,  $T$ : given an initial and goal point for the  
244 path, the FMM is applied using the goal point as a wave source. The  
245 wave propagates according to the velocities map  $F$ . The propagation  
246 is stopped once the start point of the path is reached.
- 247 • **Path extraction**: gradient descent is applied over  $T$  from the start  
248 point until the unique minimum of  $T$ , the goal point, is reached.

249 These steps are depicted in Figure 6. The main characteristics of the  
250 FM<sup>2</sup> method are path smoothness and safety in terms of obstacle clearance.

251 **4. Path optimization and trajectory evaluation**

252 An optimization methodology based on the elastic bands method [25] was  
253 designed [26]. The original concept associated with this approach appeared  
254 in the computer vision field, with the presentation of the so called “snakes”  
255 algorithm [27]. A snake is a deformable curve guided by artificial forces that  
256 pull it towards image features such as lines and edges. The solution herein

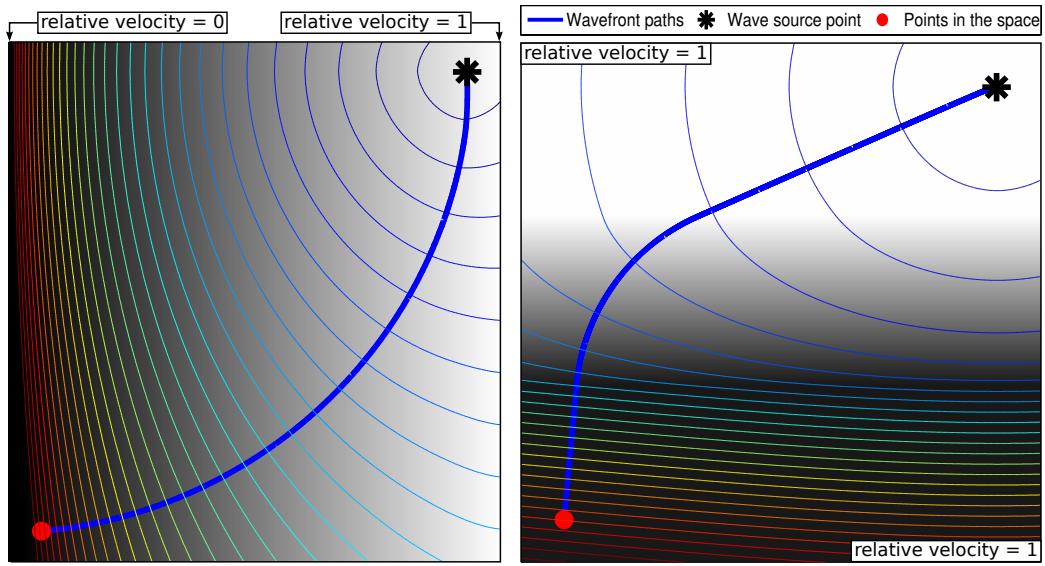


Figure 5: Examples of the geodesic paths obtained when there is a continuous gradient in the wave propagation velocities.

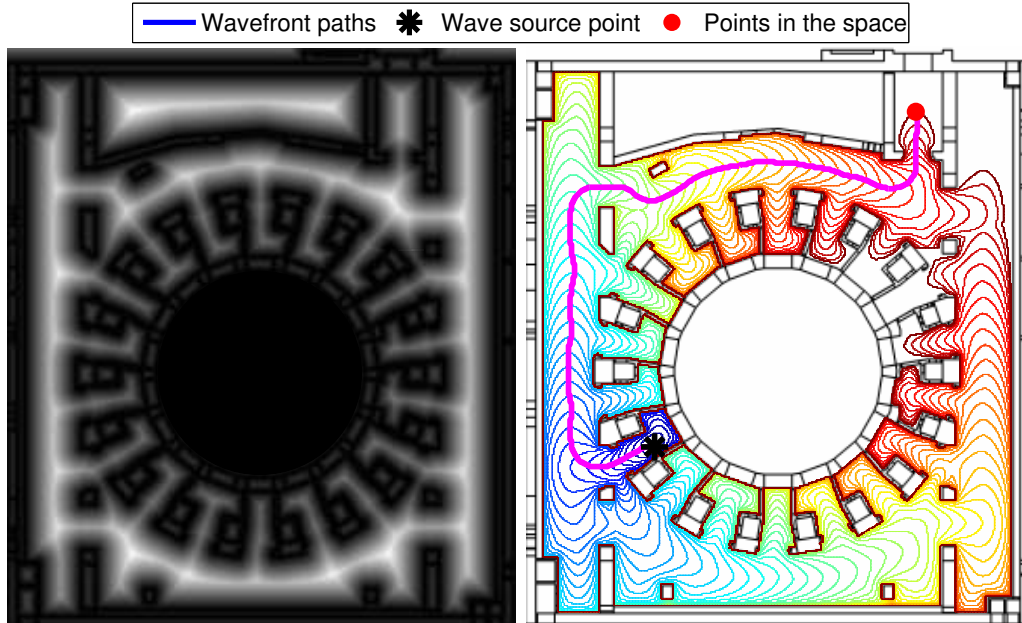


Figure 6: Velocities map for the level B1 of TB (left) and the times-of-arrival map over the initial binary map and the resulting path from the lift to the port 11 (right).

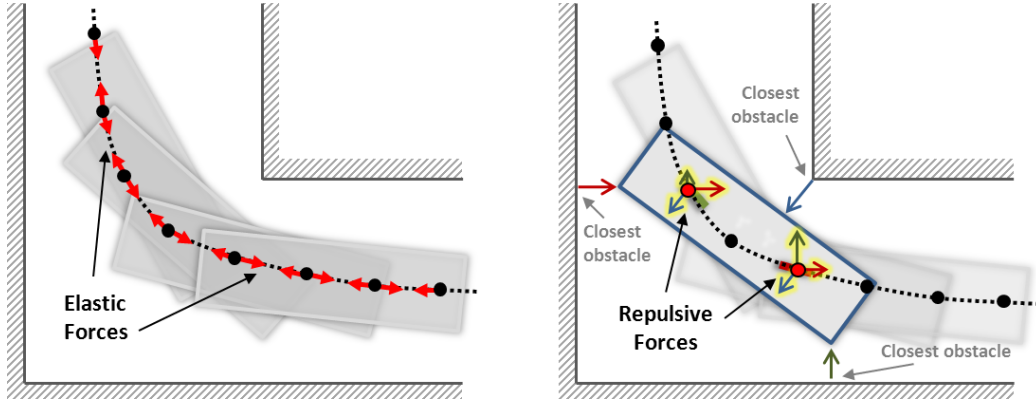


Figure 7: Elastic band concept: elastic forces to smooth the path (left) and repulsive forces generated by the closest obstacles (right).

257 proposed with the elastic bands methodology is similar to the snakes ap-  
 258 proach. Instead of retracting a curve to image features, in the path planning  
 259 problem, it repels the path out from obstacles. Following this approach, the  
 260 path is modeled as an elastic band which can be compared to a series of  
 261 connected springs subjected to two types of forces, as illustrated in Figure 7:

- 262 • Internal forces or elastic forces: the internal contraction force simulates  
 263 the Hooke's elasticity concept [28, 29], i.e., the magnitude force is pro-  
 264 portional to the amplitude of displacement. This modeling approach  
 265 allows the simulation of the behavior of a stretched band. This is the  
 266 reason why the paths become retracted and shorter.
- 267 • External forces or repulsive forces: the obstacle clearance is achieved  
 268 using repulsive forces to keep the path, and consequently the vehicle,  
 269 away from obstacles.

270 When submitted to these artificial forces, the elastic band is deformed  
 271 over time becoming a shorter and smoother path, increasing clearance from  
 272 obstacles. Hooke's law evaluates the elastic force  $F_e$  applied to path point  $P_i$   
 273 as

$$F_e(P_i) = k_e \cdot [(P_{i-1} - P_i) - (P_i - P_{i+1})] \quad (8)$$

274 where  $k_e$  is the elastic gain and  $P_{i-1}$  and  $P_{i+1}$  are the path points adjacent  
 275 to  $P_i$ . The elastic band behavior can be controlled through  $k_e$ . The band  
 276 stretches with high values of  $k_e$  while low values increase the band flexibility.

277 To determine the external forces, a collision detector algorithm is used  
 278 to evaluate the nearest obstacle point (OP) to each vehicle pose. The use  
 279 of a single OP to determine the repulsive forces may not be satisfactory to  
 280 maintain clearance from obstacles, and therefore, a larger set of obstacle  
 281 points, such as the k-nearest (k-OPs), must be considered, as illustrated in  
 282 Figure 7. This leads to a more balanced repulsive contribution ensuring  
 283 effectiveness on most situations.

284 The repulsive force for each  $P_i$  is determined as a combination of different  
 285 repulsive contributions

$$F_r(P_i) = k_r \cdot \sum_{l=\{F,R\}} \sum_{k=1}^K r_{l,k}(P_i) \quad (9)$$

286 where  $k_r$  is the repulsive gain,  $F$  and  $R$  the front and rear wheels and  $r_{l,k}$   
 287 the inverse of the distance between the k-OPs and the vehicle, considering  
 288 the front and rear wheels, as detailed in [8].

289 Once the elastic (8) and the repulsive (9) forces are computed, an update  
 290 equation procedure that defines the path evolution along each iteration is  
 291 applied as

$$P_{i,new} = P_{i,old} + k \cdot F_{total}(P_{i,old}) \quad (10)$$

292 where  $k$  is a normalization factor adding up the total force contribution  
 293 applied to all points  $P_{i,old}$  and the total force contribution is given by

$$F_{total}(P_{i,old}) = F_e(P_{i,old}) + F_r(P_{i,old}) \quad (11)$$

294 Under the influence of these artificial forces, the elastic band is deformed  
 295 over time becoming a shorter and smoother path. The stopping criteria  
 296 is defined by detecting that the magnitude changes on  $F_{total}$  are smaller  
 297 than a given threshold and by setting a maximum number of iterations.  
 298 The path optimization is thus carried out by a path deformation approach  
 299 where the computed paths are treated as flexible and deformable bands.  
 300 Elastic interactions smooth the path by removing any existing slack, whereas  
 301 repulsive forces improve clearance from obstacles by pushing away the points  
 302 of the path.

303 The output of the path optimization is a collision free path suitable for  
 304 execution. Then, the optimized paths are parametrized in terms of veloci-  
 305 ties, converting the paths into trajectories. Since the safety requirements are  
 306 mandatory and the risk of collision shall be reduced in the cluttered environ-  
 307 ment, an initial approach defines the vehicle speed profile as a function of the

308 distance to the obstacles. The velocity assumes low values when the vehicle is  
309 closer to the obstacles. Otherwise, the velocity is higher, under safety levels.  
310 To generate this initial speed profile, the minimum distance from the vehicle  
311 to the closest obstacle is identified for each point in the optimized path.

312 A maximum and minimum allowable speed are set to this profile, in order  
313 to integrate kinematic constraints. The safety margin identifies the threshold  
314 distance above which the maximum speed is considered. The speed profile  
315 thus obtained is saturated when the distance is above the threshold or below  
316 the safety margin and is referred as C-based speed profile [9]. However,  
317 the C-based speed profile is unable to handle vehicle dynamics constraints,  
318 meaning that the constraints on the admissible accelerations of the vehicle are  
319 ignored. To sidestep this issue, it has been developed a specific routine, which  
320 tests each one of the C-based speed profile transitions, checking whether the  
321 accelerations are feasible or not. Whenever a dynamic unfeasible transition  
322 is found (e.g., the calculated acceleration is out of the admissible bounds),  
323 the routine corrects the speed accordingly.

324 The output of the entire process, summarized in Figure 8, is an optimized  
325 path in terms of distance and smoothness, with a speed profile, assuming that  
326 the vehicle starts and ends with velocity equal to zero.

## 327 5. Simulated Results

328 The algorithms were implemented in MATLAB environment and inte-  
329 grated in the specially designed software tool Trajectory Evaluator and Sim-  
330 ulator (TES). The TES receives the models of the buildings, generates tra-  
331 jectories using line guidance, evaluates the resulted 3D volume swept by the  
332 vehicle along the optimized paths and exports the optimized trajectories and  
333 the corresponding 3D swept volume directly to the CAD software. The TES  
334 provides also a GUI to preview the trajectory optimization, to manipulate  
335 the scenarios, to easily choose the vehicle typology to be used in the sim-  
336 ulation and to generate results. The output of TES is a set of optimized  
337 trajectories which were validated by an independent software developed by  
338 ASTRIUM SAS [30]. The results achieved by the algorithms implemented in  
339 TES applied in the models of the real scenarios were important to proceed  
340 with the construction of the Tokamak Building.

341 The line guidance algorithm, using the FM<sup>2</sup> and the elastic bands op-  
342 timization, was applied and tested in some levels of the TB and HCB to  
343 generate trajectories. Each optimized trajectory corresponds to a nominal

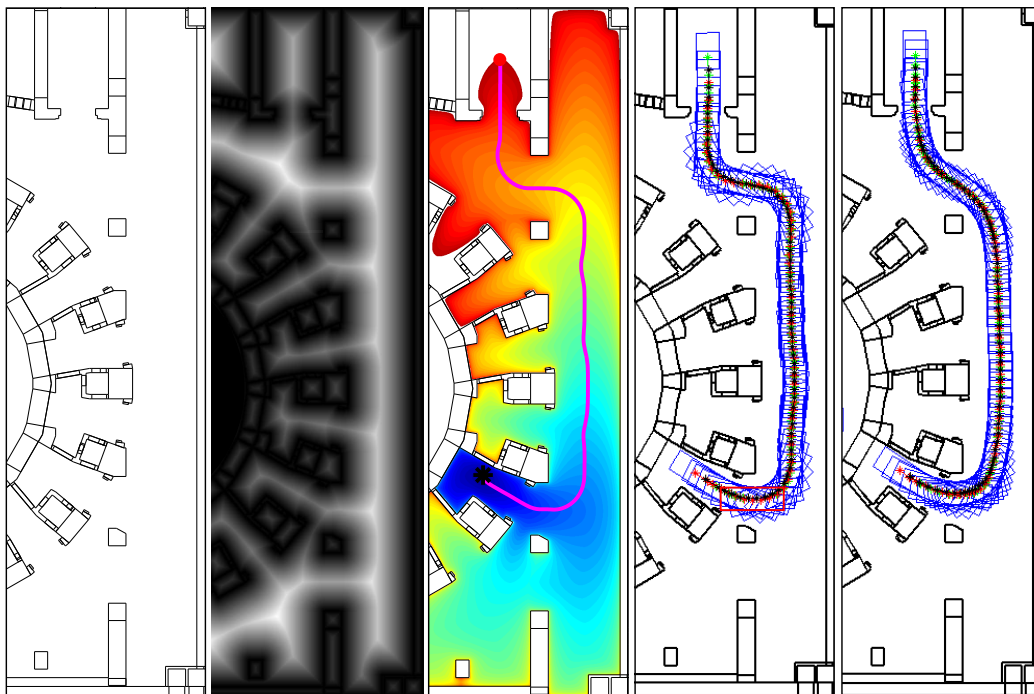


Figure 8: Steps of the proposed method on level TB/B1 (from left to right): initial map, velocities map, times-of-arrival map and FM<sup>2</sup> path, FM<sup>2</sup> path evaluated with the cask with a collision, and path after the the optimization.



344 operation of transportation between the lift and a port in the TB or a park-  
345 ing place in the HCB. Each mission only constrains the initial and final poses  
346 (positions and orientations) of the vehicle. A path is considered feasible when  
347 the minimum distance between the vehicle and the closest elements of the  
348 scenario is above a safety margin. This minimum clearance is only allowed  
349 to be infringed when entering/exiting the lift and in the docking phase.

350 First, an individual result of the optimization procedure is included before  
351 proceeding with the full results. This example is a mission from the lift to the  
352 port 10 of the level L1 of the TB, since it is one of the most complicated cases.  
353 Figure 9 shows that the FM<sup>2</sup> initialization contains points in the path with  
354 collisions, since the standard FM<sup>2</sup> in 2 dimensions does not take into account  
355 the size of the vehicle when planning. However, the optimization provides  
356 a shorter, smoother path without collisions. In Figure 10 the spanned areas  
357 for both initialization and optimization are shown. It is possible to see that  
358 the optimization has reduced the spanned area, since most of the FM<sup>2</sup> small  
359 oscillations have been reduced. Finally, Figure 11 shows the evolution of the  
360 minimum clearances and the velocities profile. Clearances are improved in  
361 those places in which the initialization had collisions. In some points of the  
362 path clearances are decreased (always above the safety margin, depicted by  
363 a dashed line) in order to reduce path length. This causes the speed profile  
364 to decrease in those places as well.

365 A total of 47 missions have been analyzed between the 2 buildings: 35  
366 missions in the TB (7 in level B1, 14 in level L1, and 14 in level L2) and 12  
367 in the HCB (7 in level L1 and 5 in level B2). Different metrics are used for  
368 both initialization and optimization: path length, swept area, total vehicle  
369 rotation angle, estimated execution time and minimum clearance along the  
370 path. The results of these metrics, except clearance, are shown in Figure 12.

371 The optimization procedure has reduced the path length in all cases. Also  
372 the swept area has been optimized in all the missions. The total steered an-  
373 gle by the vehicle is also significantly reduced since most of the oscillations  
374 created by the FM<sup>2</sup> initialization have been eliminated. However, it is in-  
375 creased in 3 missions in the TB and in all missions in the HCB/L1. These  
376 cases corresponds to sharp curves in confined spaces in which the only option  
377 for the vehicle is to get a better angle by first turning to the opposite side.  
378 As a counterpart, the estimated path execution time has been increased in  
379 all cases.

380 Smoothness require a more careful analysis. The smoothness metric em-  
381 ployed creates triangles formed by consecutive path segments and compute

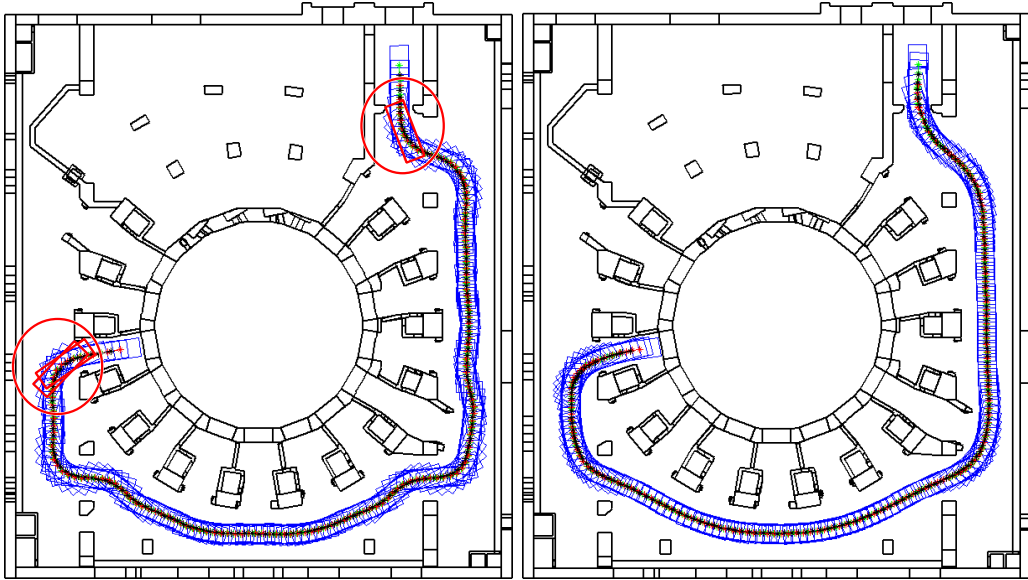


Figure 9: The path evaluation from the lift to the port 10 in level L1 of TB: the results from the initialization step (left) and from the optimization step (right).

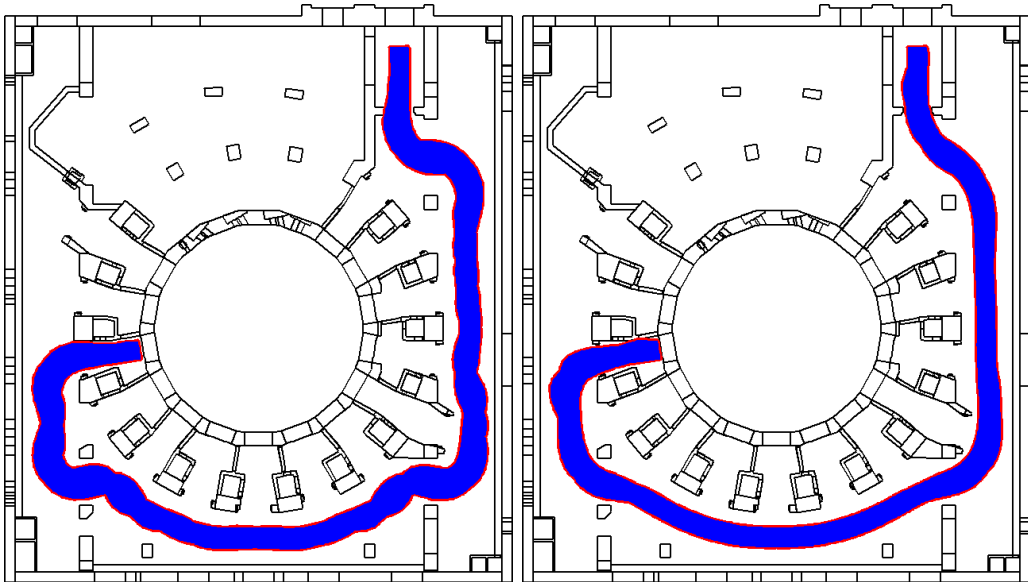


Figure 10: The spanned areas along the initialized path (left) and along the optimized path (right), from the lift to the port 10 in level L1 of TB.

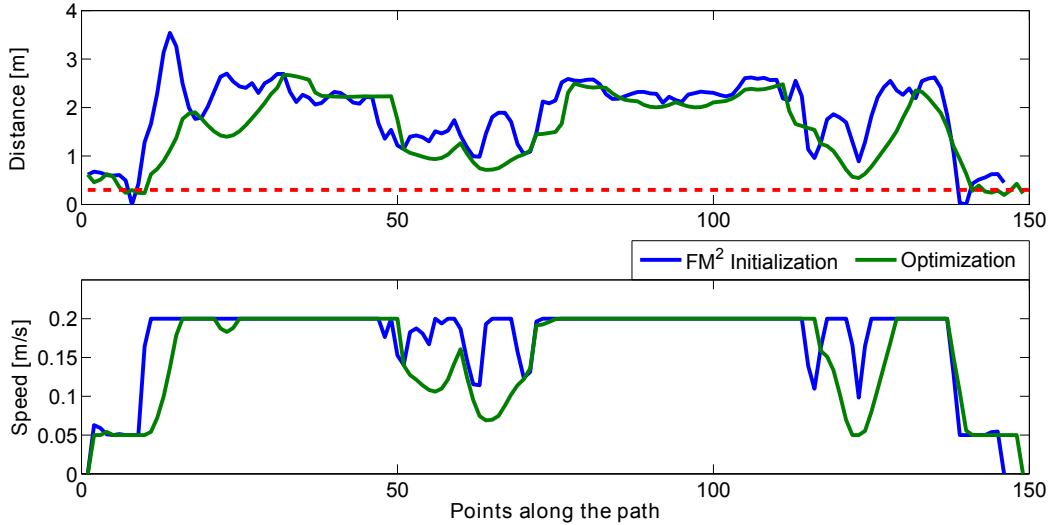


Figure 11: The minimum distance between the vehicle and the closest obstacles (top) and the speed of the vehicle (bottom) along the optimized path, from the lift to the port 10 in level L1 of TB.

382 the angle between those segments using the Pythagoras' theorem. Then,  
 383 its conjugate angle is normalized by the path segment. Finally, all the nor-  
 384 malized angles along the path are added. The higher this value is, the less  
 385 smooth the path is. Minimum value is 0 for a straight line and there is no  
 386 maximum value. Therefore, it is important that both initial and optimized  
 387 paths have the same number of points. Otherwise, the comparison would not  
 388 be fair. This metric is formally defined in equation 12:

$$smoothness = \sum_{i=2}^{n-1} \left( \frac{2 \left( \pi - \arccos \left( \frac{a_i^2 + b_i^2 - c_i^2}{2a_i b_i} \right) \right)}{a_i + b_i} \right)^2 \quad (12)$$

389 where  $a_i = dist(s_{i-2}, s_{i-1})$ ,  $b_i = dist(s_{i-1}, s_i)$ ,  $c_i = dist(s_{i-2}, s_i)$ ,  $s_i$  is the  
 390  $i^{th}$  state along the path, and  $dist(s_i, s_j)$  gives the distance (Euclidean in this  
 391 case) between states  $i$  and  $j$ .

392 Smoothness results are shown in Figure 13. Smoothness is worsened in  
 393 all cases. However, this is not an actual negative result. Note that the  
 394 smoothness values for the initial FM<sup>2</sup> paths is low (highly smooth). How-  
 395 ever, these paths present collisions. Therefore, the optimization procedure  
 396 decreases smoothness only as much as required in order to satisfy the clear-

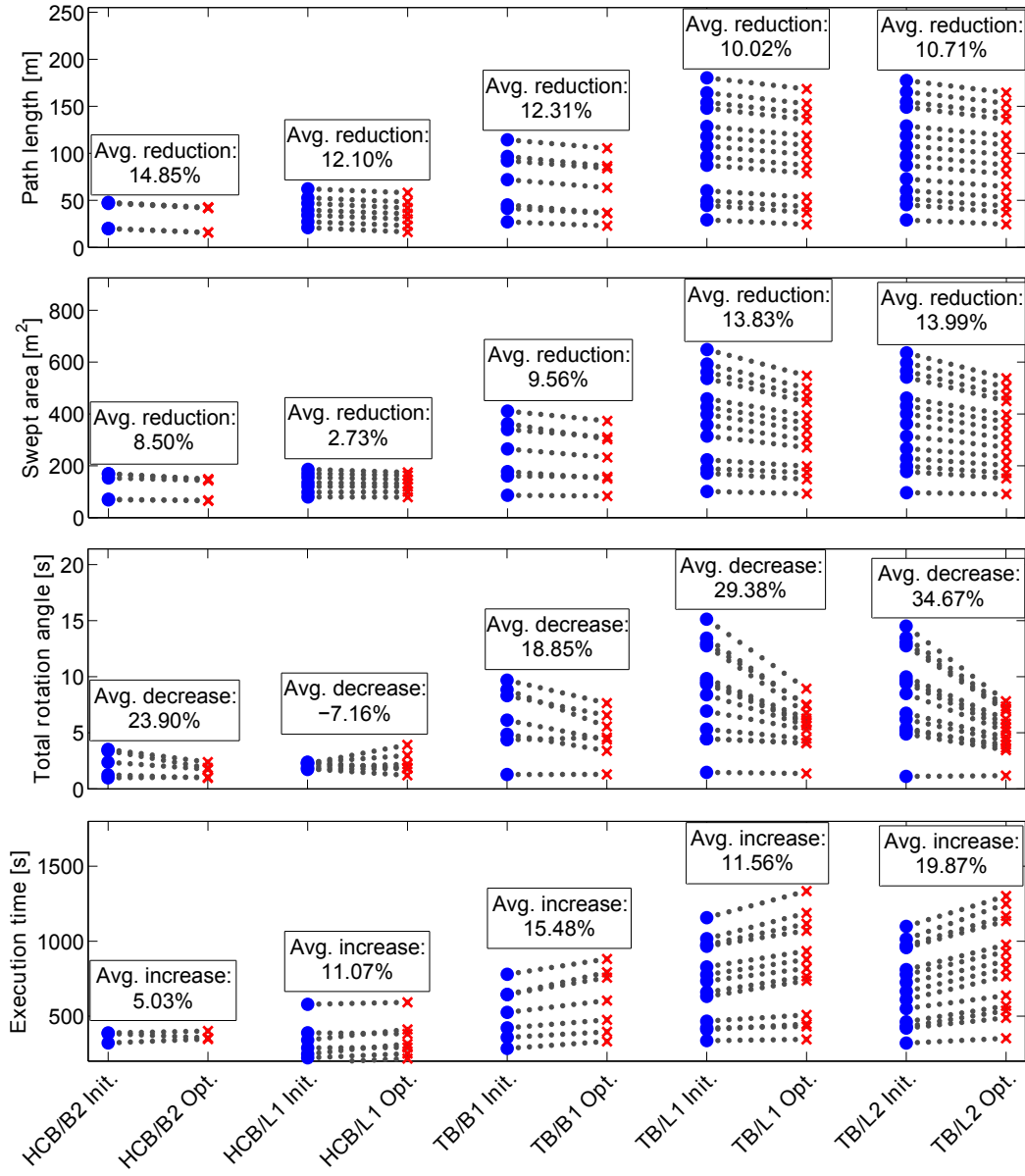


Figure 12: Metrics comparison for different levels in TB and HCB: initialization (Init.) versus optimization (Opt.).

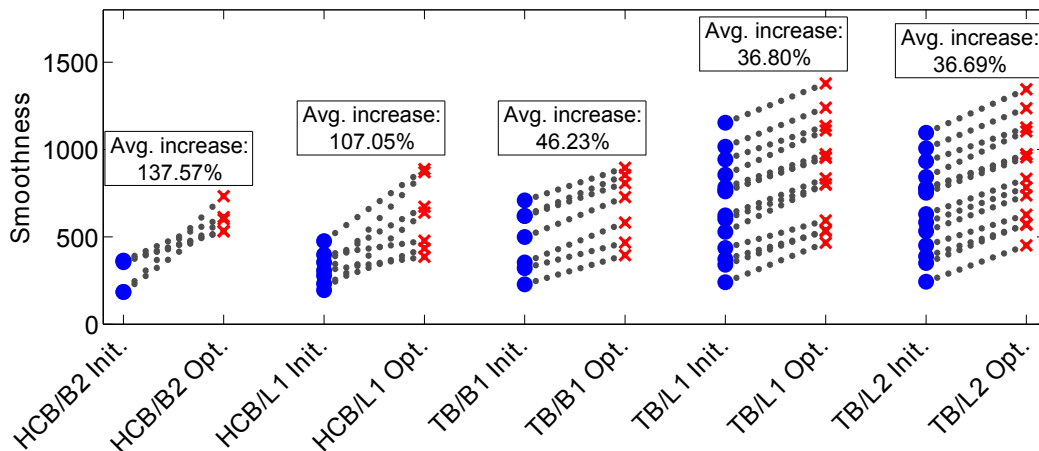


Figure 13: Smoothness metric comparison for different levels in TB and HCB: initialization (Init.) versus optimization (Opt.).

397 ance requirements.

398 The optimization provokes a redistribution of the minimum clearance  
 399 along the trajectories which have to be carefully analyzed. Table 1 shows  
 400 that the percentage of points with clashes have been reduced to 0 in all TB  
 401 levels. However, the amount of points below the minimum clearance (0.3m)  
 402 have increased. In TB there are two critical places in which it is not possible  
 403 to accomplish this restriction: the lift exit and the docks gate. Therefore,  
 404 the optimization *sacrifices* points in the surroundings of those critical places  
 405 in order to avoid clashes by bringing them closer to the obstacles. This  
 406 allows paths to have longer but smoother curves. The FM<sup>2</sup> method provides  
 407 paths close to the optimal in terms of obstacle clearance. However, the  
 408 optimization, in order to reduce oscillations and path length, decreases the  
 409 clearance also in some of the points which are already far from obstacles.  
 410 Thus, the percentage of points with clearance higher than a meter decreases  
 411 while the group between 0.5-1m increases.

412 Figure 14 illustrates how close the path returned by the FM<sup>2</sup> is to the  
 413 final solution and how fast the optimization is. As described in Section 1,  
 414 a path is a set of 2D Cartesian points. During the optimization, each point  
 415 *moves* as a result of the elastic and repulsive forces. Figure 14 presents, along  
 416 the z-axis, the distance between each point and its final position, along the  
 417 iterations represented in the x-axis. The y-axis represents the sequence of  
 418 the points of the path. At iteration 30, the distance at all points are zero,

Table 1: Clearance distributions for the initialization ( $X_i$ ) and optimized ( $X_o$ ) trajectories.

Map / Level	Clash	(0, 0.3)m	[0.3, 0.5)m	[0.5, 1)m	[1, $\infty$ )m	
HCB	B2 <sub>i</sub>	0 %	5.48 %	2.74 %	44.52 %	47.26 %
	B2 <sub>o</sub>	0 %	2.91 %	5.81 %	42.44 %	48.84 %
	L1 <sub>i</sub>	0.82 %	2.45 %	3.67 %	47.35 %	45.7 %
	L1 <sub>o</sub>	0 %	3.69 %	4.43 %	43.17 %	50.21 %
TB	B1 <sub>i</sub>	1.14 %	3.42 %	3.42 %	23.29 %	68.72 %
	B1 <sub>o</sub>	0 %	4.26 %	9.36 %	36.17 %	50.21 %
	L1 <sub>i</sub>	1.49 %	1.8 %	2.82 %	14.58 %	79.31 %
	L1 <sub>o</sub>	0 %	6.6 %	4.83 %	24 %	64.57 %
	L2 <sub>i</sub>	0.66 %	0.88 %	2.86 %	19.03 %	76.57 %
	L2 <sub>o</sub>	0 %	2.75 %	4.48 %	36.3 %	56.47 %

419 since the optimized path was achieved and the points do not move anymore  
 420 (or the oscillations are not perceptible, e.g., below a small threshold value).  
 421 Figure 14 presents large distance values in the points that correspond to the  
 422 areas of the scenario with more clearance. In the places where the scenario  
 423 is very narrow, the points are stuck along all the iterations.

424 Figure 15 presents all the missions to the level L1 of TB. Figure 15 - left  
 425 shows the paths resulted from the FM<sup>2</sup> algorithm applied to all ports. The  
 426 paths are close to the optimized solutions, but with some clashes identified  
 427 by circles. Figure 15 - right shows all the optimized paths. In some situ-  
 428 ations, as in the mission to port 11, the clearance of the path returned by  
 429 the FM<sup>2</sup> in the vicinity of the pillars is greater when compared to the opti-  
 430 mized path to the same port. However, the optimized path has no collision  
 431 in the entrance to the same port while satisfying the clearance constrains.  
 432 Figure 16 includes all the trajectories studied for the HCB. In this case the  
 433 optimization is not essential in most cases since there are not clashes in most  
 434 of the trajectories. However, optimization is applied in order to guarantee  
 435 that the requirements are accomplished. Figure 16 - right shows the effect  
 436 the optimization algorithm has in very cluttered scenarios: before entering  
 437 the parking place, the cask has to get away from the wall in order to obtain  
 438 a better angle to enter. As result, the total rotation angle is incremented.

439 Finally, an interesting point is raised. Different scenarios require different

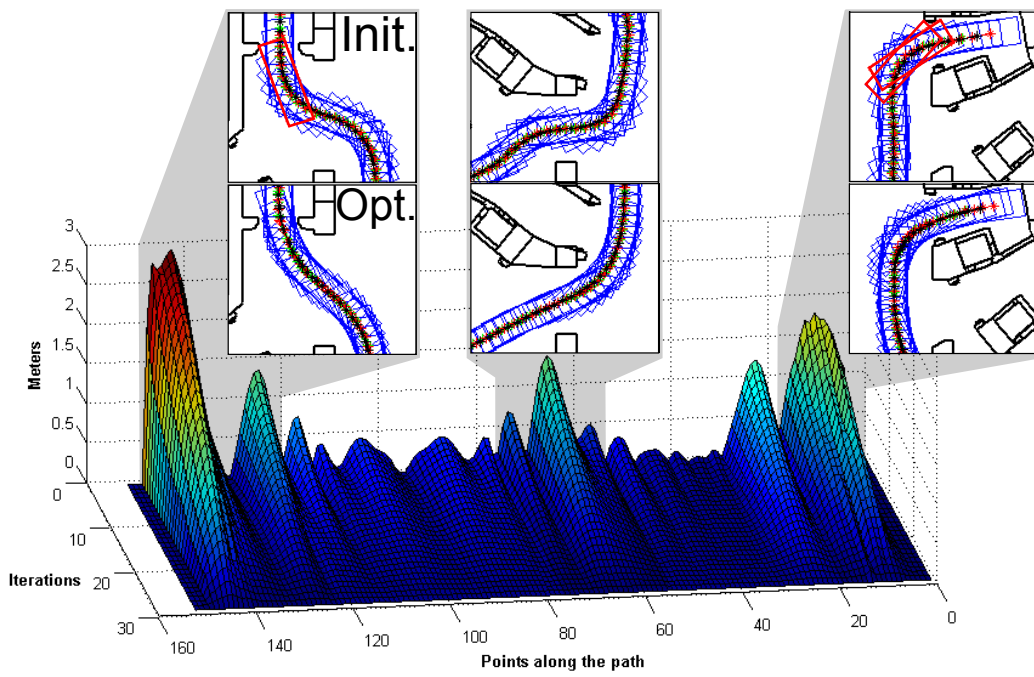


Figure 14: Evaluation of the distances between each point of the path along the iterations and its final value in the optimized path.

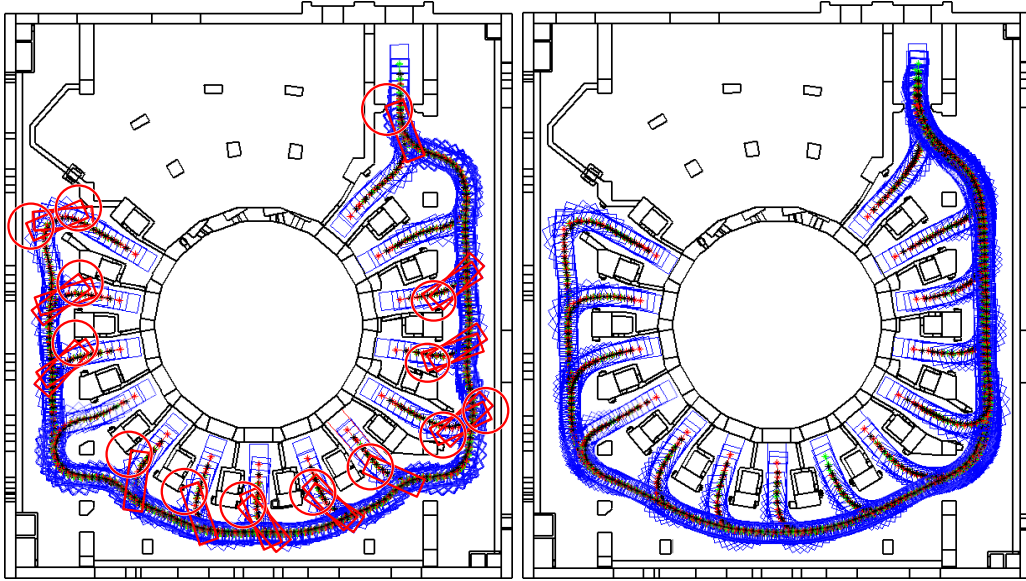


Figure 15: The path evaluation from the lift to all ports in level L1 of TB: the results from the initialization step (left) and from the optimization step (right).

440 FM<sup>2</sup> velocities maps. However, for small modifications in the scenario it  
 441 is not necessary to recompute the velocities map, since the optimization  
 442 procedure will successfully adapt the path. For instance, Figure 17 - left  
 443 shows an optimized path between the lift and a parking place where the  
 444 initial map and the respective velocity map did not considered the parked  
 445 vehicle. Running again the optimization algorithm, the new optimized path  
 446 is still smooth, but without clashes, as illustrated in Figure 17 - right.

447 The parameters  $k_e$  and  $k_r$  play an important rule for tuning the final  
 448 trajectory in terms of shortness and smoothness. The  $k_e$  regulates the elastic  
 449 path behavior. Higher values increase the path shortness approaching the  
 450 path points connectivity. Lower values allow to increase path flexibility to  
 451 obstacle-repulsive deformation. Outsized values either make the deforma-  
 452 tion process unstable or compromise path clearance. The  $k_r$  controls the  
 453 repulsion behavior by determining the preponderance of the repulsive forces  
 454 from obstacles. Gain increase allows to improve path clearance. Outsized  
 455 values conflict with path smoothness and connectivity. These parameters  
 456 were largely tested in several scenarios with similar dimensions and layout  
 457 of ITER and the best results, as the ones depicted in the previous figures,  
 458 were achieved with values of  $k_e$  and  $k_r$  between  $[0.3; 0.4]$  and  $[0.05; 0.01]$ ,



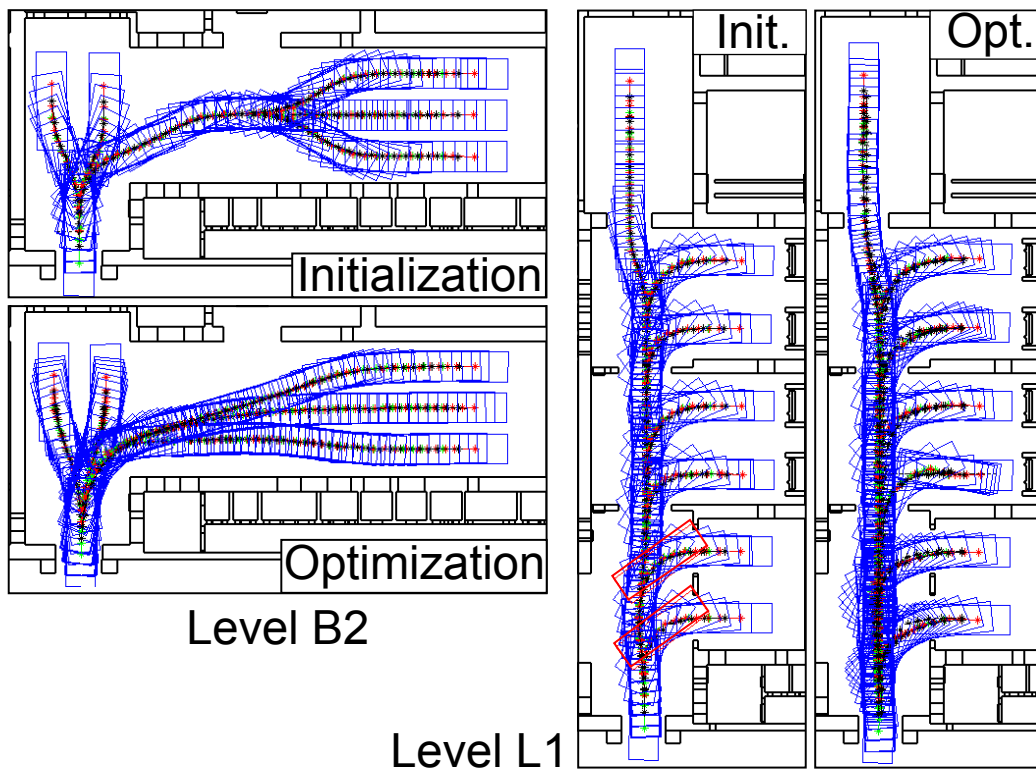


Figure 16: Path initialization and optimization from the lift to main parking places in levels L1 and B2 of HCB.

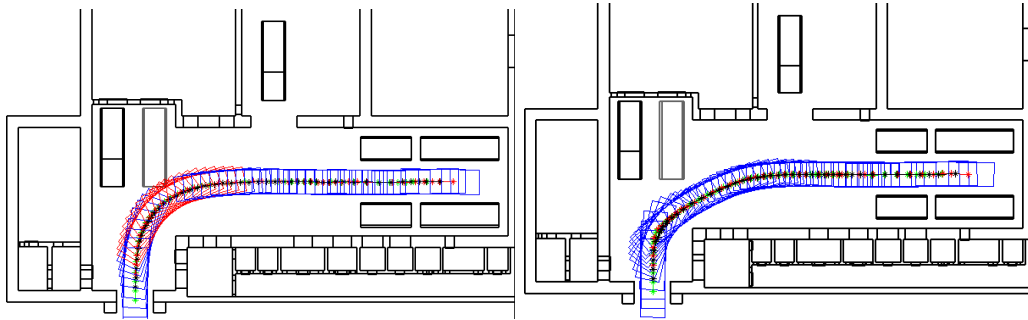


Figure 17: Path for a parking place in level B2 of HCB, in collision with a temporary vehicle (left), and the re-optimization of the path without the need of the initialization step (right).

459 respectively.

460 Lastly, the proposed framework allows to include trajectories with ma-  
 461 neuvres [10], as shown in Figure 18. So far, the maneuver poses have to be  
 462 manually defined and they will not be modified by the optimization proce-  
 463 dure. This allows to increase clearance, find feasible paths where it was not  
 464 possible before, and to accomplish restrictions about the orientation of the  
 465 final poses within the ports.

## 466 6. Conclusions

467 This paper presented a summary of an algorithm to optimize trajectories  
 468 in terms of clearance, smoothness and execution time. The algorithm has  
 469 three steps: the initialization based on the FM<sup>2</sup>, the path optimization using  
 470 rigid body dynamics and the trajectory evaluation, where a velocity profile  
 471 is created attending the clearance and maximum/minimum velocities and  
 472 accelerations. The inputs of the 2D path planning algorithm are: the vehicle  
 473 dimensions, the map of the environment and the initial and final goals of each  
 474 mission. The path initialization is fast, robust and close to the final solution.  
 475 Comparing with other previous approaches developed and tested by the same  
 476 authors, using CDT [8], or Rapidly exploring Random Tree (RRT) [31], or  
 477 only FM<sup>2</sup> [10], the algorithm proposed in this paper also provides trajectories  
 478 with no clashes whenever possible, but with better performance in terms of  
 479 computation time, smoothness and safety.

480 The algorithm was extensively tested using the maps of the ITER test  
 481 facility: a structured, but complex and cluttered scenario. More experiments

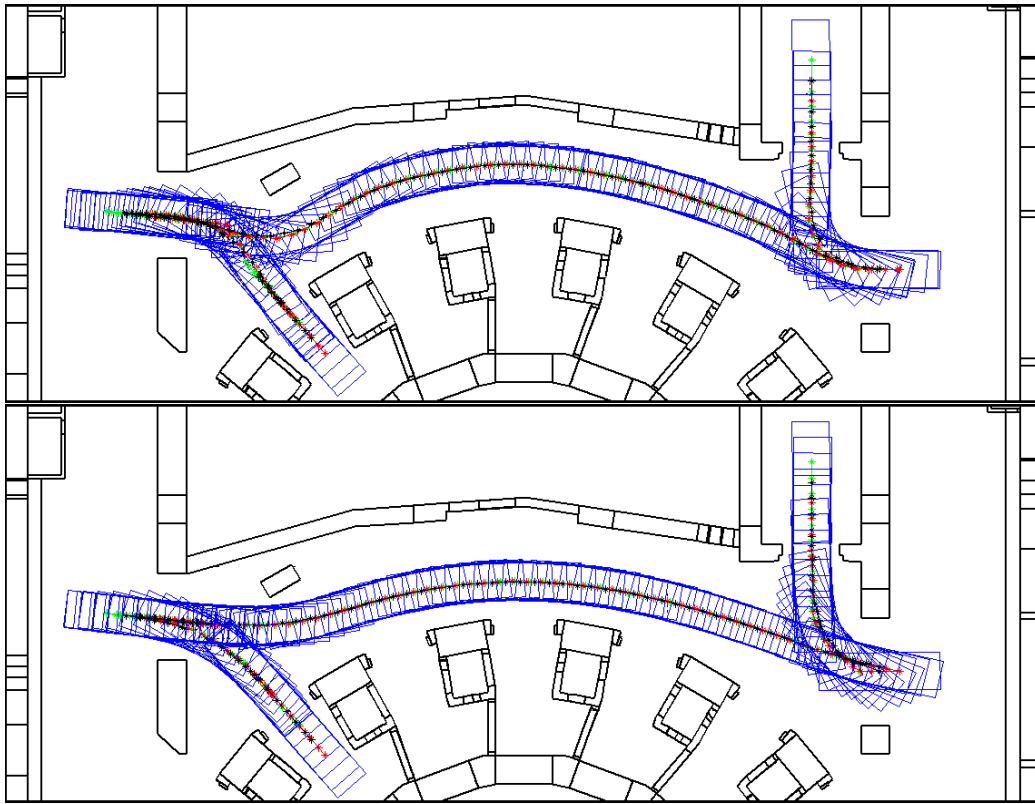


Figure 18: Example of a double maneuver in level B1 of TB, port 7: initialization (top) and optimization (bottom).

482 were done in the reactor building, since it is the core of the ITER. Results  
483 show how robust and flexible outputs are. The algorithm is also applicable  
484 to other environments, such as warehouses and using other vehicle kinematic  
485 configurations.

486 The future work focuses on extending the algorithm to a free roaming level  
487 (wheels do not follow the same path) avoiding the inclusion of maneuvers.

## 488 **Acknowledgment**

489 This work was supported by the TECHNOFUSION R&D program funded  
490 by the Community of Madrid, project DPI2010-17772 funded by the Spanish  
491 Ministry of Science. IST activities received financial support from “Fundação  
492 para a Ciência e Tecnologia” through project Pest-OE/SADG/LA0010/2013.  
493 The views and opinions expressed herein do not necessarily reflect those of  
494 the European Commission.

495 The authors want to gratefully acknowledge the comments on this work  
496 by David Álvarez and the reviewers and the audience of the ICRA 2013  
497 conference. Also, the authors acknowledge the valuable contribution of future  
498 comments by the reviewers to improve both the research and the paper.

## 499 **References**

- 500 [1] A. Tesini, J. Palmer, The ITER remote maintenance system, *Fusion*  
501 *Eng. Des.* 83 (2008) 7–9.
- 502 [2] I. Ribeiro, P. Lima, P. Aparício, R. Ferreira, Conceptual Study on  
503 Flexible Guidance and Navigation for ITER Remote Handling Transport  
504 Casks, in: *Proc. 17th IEEE/NPSS Symp. Fusion Eng.*, 1997, pp. 969–  
505 972.
- 506 [3] I. Ribeiro, P. Lima, P. Aparício, R. Ferreira, Active Docking of a Trans-  
507 port Cask Vehicle Subject to 6 Degrees of Freedom Misalignments, in:  
508 *Proc. 17th IEEE/NPSS Symp. Fusion Eng.*, 1997, pp. 973–976.
- 509 [4] G. Dudek, M. Jenkin, *Computational Principles of Mobile Robotics*,  
510 Cambridge University Press (2 edition) (2010).
- 511 [5] B. R. Sarker, S. S. Gurav, Route planning for automated guided vehicles  
512 in a manufacturing facility, *Int. J. Prod. Res.* 43 (2005) 4659–4683.

- 513 [6] H. Martínez-Barberá, D. Herrero-Pérez, Autonomous navigation of an  
514 automated guided vehicle in industrial environments, *Robot. Cim-Int.*  
515 *Manuf.* 26 (2010) 296–311.
- 516 [7] B. Trebilcock, Automatic guided vehicle basics, *Mod. Mater. Handl.* 62  
517 (2007) 46–50.
- 518 [8] D. Fonte, F. Valente, A. Vale, I. Ribeiro, A Motion Planning Method-  
519 ology for Rhombic-like Vehicles for ITER Remote Handling Operations,  
520 *Proc. 7th IFAC Symp. Intell. Autonomous Vehicles* (2011) 106–111.
- 521 [9] F. Valente, A. Vale, D. Fonte, I. Ribeiro, Optimized Trajectories of the  
522 Transfer Cask System in ITER, *Fusion Eng. Des.* 86 (2011) 1967–1970.
- 523 [10] J. Gómez, A. Vale, F. Valente, J. Ferreira, S. Garrido, L. Moreno,  
524 Fast Marching in motion planning for rhombic like vehicles operating  
525 in ITER, *Proc. IEEE Int. Conf. Rob. Aut.* (2013) 5513–5518.
- 526 [11] S. Garrido, L. Moreno, M. Abderrahim, D. Blanco, FM2: A Real-time  
527 Sensor-based Feedback Controller for Mobile Robots, *Int. J. Robot.*  
528 *Autom.* 24 (2009) 3169–3192.
- 529 [12] C. Petres, Y. Pailhas, P. Patron, Y. Petillot, J. Evans, D. Lane, Planning  
530 for Autonomous Underwater Vehicles, *IEEE Trans. Robot.* 32 (2007)  
531 331–341.
- 532 [13] Q. H. Do, S. Mita, H. T. Niknejad, L. Han, Dynamic and safe path  
533 planning based on support vector machine among multi moving obsta-  
534 cles for autonomous vehicles, *IEICE Transactions Inf. Syst.* 96-D (2013)  
535 314–328.
- 536 [14] Q. H. Do, S. Mita, K. Yoneda, Narrow passage path planning using  
537 fast marching method and support vector machine, in: *Proc. Vehicles*  
538 *Symposium*, 2014, pp. 630–635.
- 539 [15] R. Takei, R. Tsai, Optimal trajectories of curvature constrained motion  
540 in the hamilton-jacobi formulation, *J. Scientific Computing* 54 (2013)  
541 622–644.
- 542 [16] S. Garrido, L. Moreno, D. Blanco, F. Martin, Smooth path planning for  
543 non-holonomic robots using fast marching, in: *Proc. Int. Conf. Mecha-*  
544 *tronics*, 2009, pp. 1–6.

- 545 [17] J. Ferreira, A. Vale, I. Ribeiro, Localization of Cask and Plug Remote  
546 Handling System in ITER using multiple Video Cameras, *Fusion Eng.*  
547 *Des.* 88 (2013) 1992–1996.
- 548 [18] D. Locke, C.-G. Gutiérrez, C. Damiani, J.-P. Friconneau, J.-P. Martins,  
549 Progress in the conceptual design of the ITER cask and plug remote  
550 handling system, *Fusion Eng. Des.* 89 (2014) 2419–2424.
- 551 [19] D. Wang, F. Qi, Trajectory planning for a four-wheel-steering vehicle,  
552 in: *Proceedings of the IEEE International Conference on Robotics and*  
553 *Automation*, volume 4, 2001, pp. 3320–3325.
- 554 [20] A. Vale, D. Fonte, F. Valente, I. Ribeiro, Trajectory optimization for  
555 autonomous mobile robots in ITER, *Robotics and Autonomous Systems*  
556 62 (2014) 871–888.
- 557 [21] J. V. Gómez, *Advanced Applications of the Fast Marching Square Plan-*  
558 *ning Method*, Master’s thesis, Carlos III University of Madrid, 2012.
- 559 [22] A. Valero-Gómez, J. V. Gómez, S. Garrido, L. Moreno, The Path to Ef-  
560 ficiency: Fast Marching Method for Safer, More Efficient Mobile Robot  
561 Trajectories, *IEEE Robot. Autom. Mag.* 20 (2013) 111–120.
- 562 [23] J. A. Sethian, A Fast Marching Level Set Method for Monotonically  
563 Advancing Fronts, *Proc. Natl. Acad. Sci.* 93 (1996) 1591–1595.
- 564 [24] S. Osher, J. Sethian, Fronts Propagating With Curvature-dependent  
565 Speed - Algorithms Based On Hamilton-Jacobi Formulations, *J. Com-*  
566 *put. Phys.* 79 (1988) 12–49.
- 567 [25] S. Quinlan, O. Khatib, Elastic bands: connecting path planning and  
568 control, in: *Proc. IEEE Int. Conf. Robotics and Automation*, volume 2,  
569 1993, pp. 802–807.
- 570 [26] A. Vale, D. Fonte, F. Valente, J. Ferreira, I. Ribeiro, C. Gonzalez, Flex-  
571 ible path optimization for the Cask and Plug Remote Handling System  
572 in ITER, *Fusion Eng. Des.* 88 (2013) 1900–1903.
- 573 [27] M. Kass, A. Witkin, D. Terzopoulos, Snakes: Active contour models,  
574 *Int. J. Comp. Vis.* 1 (1988) 321–331.

- 575 [28] F. Kang, S. Zhong-Ci, *Mathematical Theory of Elastic Structures*,  
576 Springer New York, 1981.
- 577 [29] F. P. Beer, E. R. Johnston, J. T. DeWolf, *Mech. Mater.*, McGraw Hill,  
578 2002.
- 579 [30] P. Ruibanys, C. Reig, E. Gazeau, J. Marmie, N. Etchegoin, *Definition,*  
580 *Development and Operation of a Comprehensive Virtual Model of the*  
581 *ITER Buildings, ATS and TCS*, in: *26th Symp. Fusion Technology*,  
582 2010.
- 583 [31] D. Fonte, F. Valente, A. Vale, I. Ribeiro, *Path Optimization of Rhombic-*  
584 *Like Vehicles: An Approach Based on Rigid Body Dynamic.*, in:  
585 *Proceedings of the 15th IEEE International Conference on Advanced*  
586 *Robotics*, 2011, pp. 106–111.